particles

MDPI

Article

Evaluation of a Timepix3 Telescope for Applications as a Compton Scatter Polarimeter for Hard X- and Soft γ-Rays

Jindrich Jelinek [1,2,*], Benedikt Bergmann [1] and Petr Smolyanskiy [1]

[1] Institute of Experimental and Applied Physics, Czech Technical University in Prague, Husova 5, 110 00 Prague, Czech Republic
[2] Department of Nuclear and Particle Physics, University of Geneva, 24 quai Ernest-Ansermet, 1205 Geneva, Switzerland
* Correspondence: jindrich.jelinek@cvut.cz

Abstract

This work presents a simulation study of a Timepix3 telescope composed of nine detectors for use as a Compton scatter polarimeter in the energy range of 35–100 keV. Four detectors carry 1 mm thick silicon (Si) sensors and five detectors carry 1 mm thick cadmium telluride (CdTe) sensors. The modulation factor for 100% linearly polarized X-ray beams was found to be $\mu_{100} > 70\%$ in the energy range of 55–80 keV. The quality factor of the polarimeter has its maximum 12.8% at the energy 75 keV. The comparison of quality factors and the calculations of a hypothetical observation of the Crab nebula show that this multilayer Timepix3 approach is competitive with contemporary X-ray polarimeters.

Keywords: hybrid pixel detector; Timepix3; X-ray polarimetry; telescope

1. Introduction

Hard X-ray polarimetry measurements are sought in astronomy. These high-energy photons have their origins close to the compact objects (black holes, neutron stars). As such, the polarization measurements could tell us more about the accretion dynamics close to the compact object, the jet formation mechanism, or the acceleration mechanism of high-energy particles [1].

Not many X-ray polarimetry measurements have been taken in the energy range of 35–100 keV, and not many dedicated polarimeters have been built. The balloon-borne detectors PoGOLite (20–120 keV) and the newer PoGO+ (20–180 keV) measured the polarization of the Crab nebula and the X-ray binary Cygnus X-1 [2–4]. The balloon-borne telescope X-Calibur presented a measurement of the polarization of the X-ray pulsar GX 301-2 [5] in the energy range of 15–35 keV, and its successor XL-Calibur measured the polarization of the Crab nebula [6] in the energy range of 19–64 keV. The space-borne detector POLAR studied the polarization of 14 γ-ray bursts [7] in the energy range of 50–500 keV.

The paper by Jelinek et al. [8] investigated the usage of a single Timepix3 detector with a 1 mm thick silicon sensor as a Compton scatter polarimeter in the energy range of 32.5–67.5 keV in both experiment and simulation, and up to 220 keV only in simulations. The modulation factor μ_{100} of a 100% linearly polarized beam was found to be high, with its maximum $\mu_{100} > 77\%$ in the energy range of 45–80 keV. However, the efficiency of detection of the photons useful for polarimetry is low, with the maximum efficiency $\varepsilon > 0.13\%$ achieved in the energy range of 45–50 keV. The quality factor $q = \mu_{100}\sqrt{\varepsilon}$ has a maximum 2.9% at photon energy 50 keV. An obvious solution to the low efficiency is to

Check for updates

Academic Editors: Armen Sedrakian, Matteo Duranti and Valerio Vagelli

Received: 15 October 2025
Revised: 5 December 2025
Accepted: 26 December 2025
Published: 2 February 2026

Copyright: © 2026 by the authors. Licensee MDPI, Basel, Switzerland. This article is an open access article distributed under the terms and conditions of the Creative Commons Attribution (CC BY) license.

use multiple detectors. This work presents a simulation study of a hard X-ray polarimeter composed of Si and CdTe Timepix3 detectors.

2. Simulated Setup

Timepix3 [9] is a hybrid pixel detector of ionizing radiation. It features a pixel matrix 256 × 256 with a pixel pitch of 55 µm (area 1.4 × 1.4 cm^2), and it can measure the deposited energy and the time of arrival (ToA) in the pixels simultaneously. The timing resolution is 1.56 ns. Particle interactions excite one or more pixels in the sensor. The pixel hits adjacent by their edges are grouped into a single cluster. All pixels in the same cluster must have come within a given time window that we usually set in real measurements to 200 ns. However, the time window was meaningless in our simulation, as we simulated the individual primary photons to come at intervals much longer than 200 ns, and interactions within a single event happen at significantly shorter time scales.

We simulated a setup consisting of four Si and five CdTe Timepix3 detectors (Figure 1). There are four Si and one CdTe sensors in a row facing the beam. Their spacing is 4 mm. Then, there are four CdTe sensors around them in the shape of a part of a hexagon, and they are touching at their edges. All sensors had a thickness of 1 mm. This arrangement of the sensors leaves space for the hypothetical readout cards (these were not modeled), so this array of sensors could potentially be built with only minor changes at worst.

In the investigated energy range 35–100 keV, the Si sensors act as scatterers and may also act as absorbers because the cross-sections for Compton scattering and photoabsorption in silicon equal 56.9 keV. The high-Z CdTe sensors around and the one in the back are absorbers for the scattered photons that were not absorbed in the silicon, therefore boosting the efficiency of the telescope.

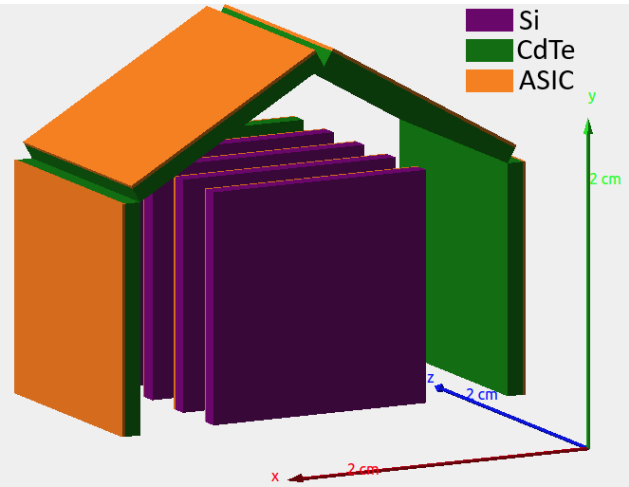


Figure 1. The simulated setup in Geant4. Four silicon sensors (purple) sit in a row with their planes perpendicular to the incoming beam. Four cadmium telluride (green) sensors are arranged around the silicon sensors to absorb the photons scattered to the sides. A single cadmium telluride sensor sits behind the silicon sensors to absorb photons scattered to the back and to enhance the imaging capability. All sensors have a thickness of 1 mm. Timepix3 ASICs of thickness 200 µm are displayed in brown color. The simulated X-ray beams traveled in the positive direction of the z-axis.

We simulated monoenergetic non-divergent X-ray beams 35–100 keV traveling along the z-axis in the positive direction (see Figure 1 for the axes definition). We simulated unpolarized beams and 100% linearly polarized beams that were polarized along the y-axis, along the x-axis, and at 45° to the two axes. The beam had a uniform square profile 0.6 × 0.6 cm^2. This would be roughly the size of the X-ray emitting part of the Crab nebula if it were imaged via an X-ray telescope with a 10 m focal length.

The propagation of particles and their interactions in the sensors were simulated in Geant4 [10] (version 11.2.0) using the physics list G4EmLivermorePolarizedPhysics. This physics list describes interactions of polarized photons from 250 eV to 100 GeV. Default settings of the physics list were used, except the maximum allowed step size which was set to 5 µm.

The charge carrier propagation through the semiconductor sensors was modeled in Allpix-2 [11] (version 3.0.0). The modeled electric field in the Si sensors was linear:

$$E(z) = \frac{|V_b| - |V_d|}{d} + 2\frac{|V_d|}{2}\left(1 - \frac{z}{d}\right), \quad (1)$$

where $V_d = 280$ V is the depletion voltage, $V_b = 400$ V is the bias voltage, $d = 1$ mm is the sensor thickness, and z is the height in the sensor measured from the pixelated electrode. Holes drifted towards the pixelated electrode in the Si sensors. The electric field in the CdTe sensors was modeled as constant $E(z) = \text{const.}$ and the bias voltage was -400 V. The detector response and the signal digitization were modeled in an in-house developed C++ code. The deposited charge from Allpix-2 is smeared by a Gaussian, and then it is compared with a threshold. A Gaussian is a good approximation of the electronics noise. The minimum energy per-pixel threshold was simulated at 3.5 keV in the Si detectors and at 4.3 keV in the CdTe detectors. This resulted in the full-width at half-maximum (FWHM) from 2.3 keV at 6 keV cluster energy to FWHM 3.8 keV at 65 keV cluster energy in the Si sensors and the FWHM from 4.9 keV at 6 keV cluster energy to FWHM 7.4 keV at 65 keV cluster energy in the CdTe sensors.

3. Method

Compton scatter polarimetry relies on Compton scattering and photoabsorption. When a photon scatters, it deposits part of its energy E_c. If the photon then deposits the remainder of its energy E_p as a photoelectron, we see two coincident events in the detectors. The sum of these two energies gives us the original energy of the photon:

$$E = E_c + E_p. \quad (2)$$

Double Compton scattering is also possible when the photon does not deposit its whole initial energy and escapes. We do not have a 100% accurate method of distinguishing double Compton scattering from Compton scattering+photoabsorption. We can use the Compton scattering kinematics:

$$\cos\theta = 1 - m_e c^2 \left(\frac{1}{E_p} - \frac{1}{E_c + E_p}\right), \quad (3)$$

where $m_e c^2 = 511$ keV is the rest energy of the electron and θ is the scattering angle. If the energies E_c, E_p are such that $\cos\theta < -1$, we can safely reject the coincident pair. Another possibility (which we did not explore in this work) is to reconstruct the Compton cone and verify if the cone orientation is consistent with the expected source position [8].

We identified coincident pairs of events that came within $\tau = 200$ ns of each other. The triple coincidences of Compton scattering, Compton scattering, and photoabsorption are negligible at lower energies, and they are less than 5% of the number of double coincidences at high energies close to 100 keV. We did not use triple or multiple coincidences in our analysis. We calculated $\cos\theta$ using Equation (3) and rejected coincident pairs with $\cos\theta < -1$. Knowing the positions of the events thanks to the fine pixelization of Timepix3, we calculated the scattering azimuthal angle φ in the plane perpendicular to the beam direction. We made a histogram of angles φ and divided it by the histogram of φ of the un-

polarized beam to remove detector geometry effects. If the investigated beam were, indeed, polarized, the ratio $f(\varphi)$ of the two histograms would carry a cosine modulation [1]:

$$f(\varphi) \propto 1 + \mu \cos(2(\varphi - \varphi_0)), \tag{4}$$

where μ is directly proportional to the degree of polarization and φ_0 is an angle at 90° to the polarization plane. The degree of polarization can be calculated:

$$P = \frac{\mu}{\mu_{100}}, \tag{5}$$

where μ_{100} is the modulation created by a 100% linearly polarized beam (also called modulation factor). The sensitivity of a polarimeter can be quantified by the minimum detectable polarization [1]:

$$\mathrm{MDP}_{99} = \frac{429\%}{\mu_{100} R_{\mathrm{src}}} \sqrt{\frac{R_{\mathrm{src}} + R_{\mathrm{bcg}}}{T}}, \tag{6}$$

where T is the duration of measurement, R_{src} is the signal rate, and R_{bcg} is the background rate. MDP_{99} tells us the level that could be exceeded by a hypothetical unpolarized source with 1% probability [1]. The smaller the minimum detectable polarization is, the more sensitive the instrument is.

4. Results

The efficiency of detection and the modulation factor μ_{100} are shown in Figure 2. The efficiency is defined as

$$\varepsilon = \frac{N_{\mathrm{pairs}}}{N_{\mathrm{incident}}}, \tag{7}$$

where N_{pairs} is the number of detected coincident pairs and N_{incident} is the number of photons in the beam. The best efficiency 3.27% was achieved at the energy 80 keV when the beam is polarized along the y-axis. The modulation factors μ_{100} are higher than 70% in the energy range 55–80 keV. The modulation factors have consistent values regardless of the beam polarization orientation, but the efficiency depends on the polarization degree of the beam because the CdTe sensors around the Si sensors do not cover a full circle. The quality factor $q = \mu_{100}\sqrt{\varepsilon}$ is shown in Figure 3 and it is >10% in the energy range of 55–100 keV. Its maximum value 12.8% occurs at the energy 75 keV if the beam is polarized along the y-axis.

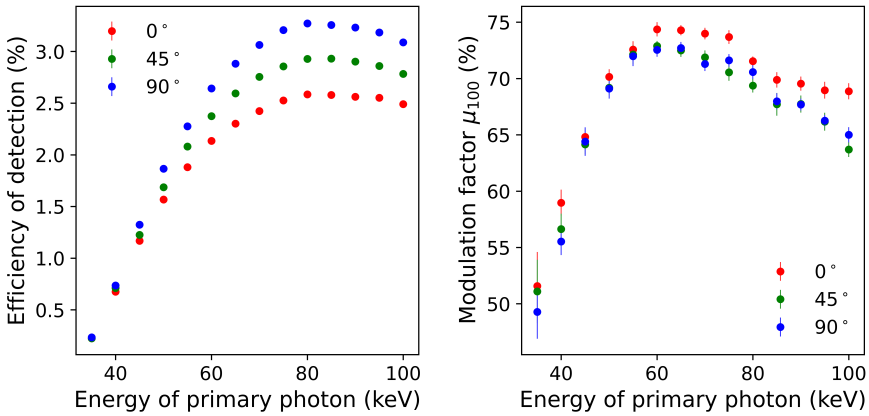


Figure 2. The (**left**) panel shows the efficiency of detection of coincidence pairs for 100% polarized X-ray beams of different energies. The (**right**) panel shows the modulation factor μ_{100} created by such a beam. Different colors represent beams polarized at different angles with respect to the x-axis. The blue and green data points overlap in part of the (**right**) figure.

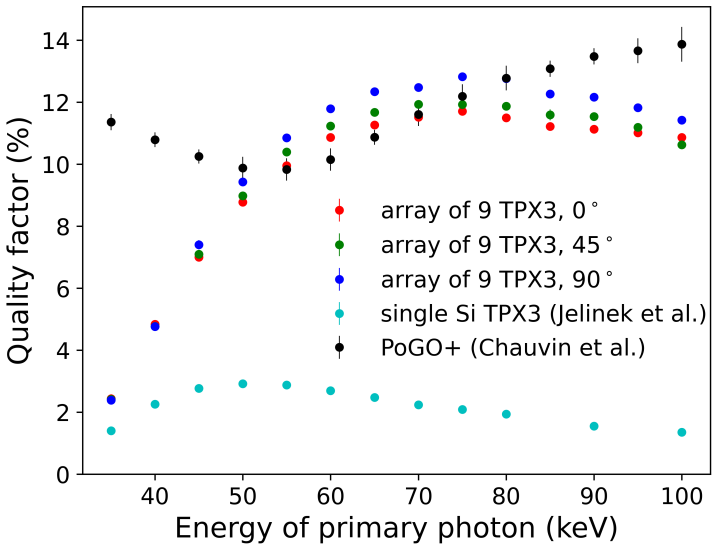


Figure 3. Quality factor (red, green, and blue dots) of the setup shown in Figure 1 for beams hitting in the positive z-axis direction. The different colors represent different polarization angles in the detector coordinate frame. For comparison, the quality factor of a single 1 mm thick Si Timepix3 from the paper [8] is shown in cyan dots, and the quality factor of PoGO+ calculated from ε and μ_{100} in the paper [12] is shown in black dots.

5. Discussion

The application of Timepix3 for X-ray polarimetry of celestial sources would require placing the detector on a high-altitude balloon or a spacecraft. The Timepix-family detectors have a long space heritage [13]. The first Timepix in open space, the experiment SATRAM, was launched in 2013 [14]. SATRAM started full operations in August 2014. Until the end of 2021, the fraction of noisy pixels stayed below 0.6% [15]. Since then, the fraction of noisy pixels has increased, but the detector is still operational. A space mission could also bring large temperature swings in the detector, changing the energy calibration, but these changes can be corrected from laboratory measurements [16–18].

Thanks to the amount of information present in each cluster (cluster shape and size, energy and ToA in each pixel), different types of particles can be easily identified, for example, by machine learning [19]. The particle classification could help a lot in background subtraction and the selection of only electron clusters.

Figure 3 shows that in the energy range 50–75 keV, the investigated Timepix3 telescope offers a quality factor comparable to, or better than, PoGO+. On top of that, if installed in the focal plane of an X-ray mirror, the Timepix3 telescope could also perform imaging thanks to its fine pixelization.

We can make a back-of-the-envelope calculation of the performance of our setup if it were placed in the focal plane of an X-ray mirror. We take the parameters of the NuSTAR mirror [20]. Let us imagine the observation of the Crab nebula, whose spectrum can be found in the paper [21]. We assume that the background rate is zero ($R_{\mathrm{bcg}} = 0$ in Equation (6)), which is the best-case scenario. Figure 4 shows the predicted MDP_{99} after a 7 d long measurement in the energy range of 35–65 keV. The lowest (best) MDP_{99} is 5.3% at the energy 50 keV. A better polarization resolution can be traded for a worse energy resolution. We can calculate the average modulation factor:

$$\mu_{\mathrm{ave}} = \frac{\sum_E \mu_{100,E} N_E}{\sum_E N_E} \tag{8}$$

where $\mu_{100,E}$ are the modulation factors and N_E are the numbers of coincident pairs in respective energy bins. We assumed that the radiation in all energy bins is polarized in the same direction. If we combined data from the full spectrum 35–65 keV captured in the figure, we could achieve $\mathrm{MDP}_{99} = 2.5\%$. This number can be compared with other X-ray polarimeters. Calibration measurements and simulations of PoGO+ predict the MDP_{99} for the Crab nebula to be 7.3% after a 7 d measurement (50% on-source, 50% off-source) [12]. Data from the X-Calibur 2018-19 campaign suggest $\mathrm{MDP}_{99} = 11.8\%(t/\mathrm{day})^{-1/2}$ for the Crab nebula, implying $\mathrm{MDP}_{99} = 4.5\%$ after a 7 d measurement [22]. However, both teams of authors took the background into account, so the results of other polarimeters are worse than if there was no background.

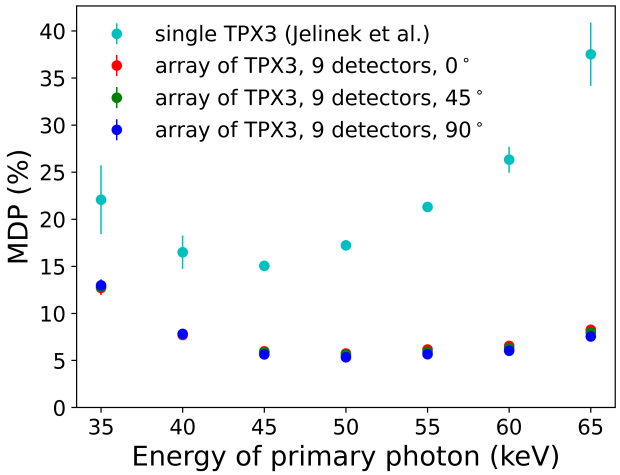


Figure 4. The minimum detectable polarization (Equation (6)) for a hypothetical observation of the Crab nebula in the focal plane of a NuSTAR mirror for 7 d under the assumption of zero background ($R_{\mathrm{bcg}} = 0$). We can compare the nine-detector telescope from this work (red, green, and blue dots) with the single 1 mm thick Si Timepix3 (cyan dots) investigated in the paper [8]. The different colors represent different polarization angles in the detector coordinate frame. Only energies up to 65 keV are shown because the NuSTAR mirror effective area quickly decreases at higher energies. The red, green, and blue dots are overlapping—there is not much difference in MDP_{99} if the radiation comes at a different polarization angle.

Another possible use case for the Timepix3 polarimeter could be in combination with Compton camera imaging. Compton camera imaging with Timepix3 has been well established in both multiple-layer [23] and single-layer [8,24–28] configurations. The polarimeter could observe bright X-ray celestial sources such as the Sun or gamma-ray bursts. The full-width at half-maximum (FWHM) of a single-layer Timepix3 Compton camera was shown to be 16–21° in the work by Jelinek et al. [8], and we expect a similar FWHM also with a telescope.

6. Conclusions

This work evaluated the performance of the telescope composed of four Si and five CdTe Timepix3 detectors (Figure 1) as a Compton scatter polarimeter in simulations in the energy range of 35–100 keV. The modulation factor μ_{100} is greater than 70% in the energy range of 55–80 keV (Figure 2). The quality factor was found to be >10% in the energy range of 55–100 keV with its maximum 12.8% at the energy 75 keV if the incoming radiation is polarized along the y-axis. The quality factor was shown to be comparable to or better than that of the PoGO+ polarimeter in the energy range of 50–75 keV (Figure 3). On top of that, fine pixelization of Timepix3 would allow for imaging if used in the focal plane of an X-ray mirror, or for Compton camera imaging of bright sources if used without a

mirror. The particle classification in Timepix3 could be used to suppress background from other types of radiation. The hypothetical setup with an X-ray mirror was compared to the PoGO+ and X-Calibur X-ray polarimeters, showing competitive values of the minimum detectable polarization in a hypothetical Crab nebula observation.

Author Contributions: J.J. performed the simulations and data analysis, and wrote the manuscript; B.B. helped with the simulated telescope design and revised the manuscript; P.S. is the author of the C++ code simulating the detector response and signal digitization in Timepix3, and helped with the simulations. All authors have read and agreed to the published version of the manuscript.

Funding: The authors B.B. and P.S. acknowledge funding from the Czech Science Foundation under Registration Number GM23-04869M.

Data Availability Statement: The simulated data files and the Python (version 3.12.10) code (in Jupyter notebooks) to analyze them are available on Zenodo (DOI: 10.5281/zenodo.17524156).

Conflicts of Interest: The authors declare no conflicts of interest.

References

1. Chattopadhyay, T. Hard X-ray polarimetry—An overview of the method, science drivers, and recent findings. *J. Astrophys. Astron.* **2021**, *42*, 106. [CrossRef]
2. Chauvin, M.; Florén, H.G.; Jackson, M.; Kamae, T.; Kawano, T.; Kiss, M.; Kole, M.; Mikhalev, V.; Moretti, E.; Olofsson, G.; et al. Observation of polarized hard X-ray emission from the Crab by the PoGOLite Pathfinder. *Mon. Not. R. Astron. Soc. Lett.* **2015**, *456*, L84–L88. [CrossRef]
3. Chauvin, M.; Florén, H.G.; Friis, M.; Jackson, M.; Kamae, T.; Kataoka, J.; Kawano, T.; Kiss, M.; Mikhalev, V.; Mizuno, T.; et al. Shedding new light on the Crab with polarized X-rays. *Sci. Rep.* **2017**, *7*, 7816. [CrossRef]
4. Friis, M.; Kiss, M.; Mikhalev, V.; Pearce, M.; Takahashi, H. The PoGO+ Balloon-Borne Hard X-ray Polarimetry Mission. *Galaxies* **2018**, *6*, 30. [CrossRef]
5. Abarr, Q.; Baring, M.; Beheshtipour, B.; Beilicke, M.; de Geronimo, G.; Dowkontt, P.; Errando, M.; Guarino, V.; Iyer, N.; Kislat, F.; et al. Observations of a GX 301–2 Apastron Flare with the X-Calibur Hard X-Ray Polarimeter Supported by NICER, the Swift XRT and BAT, and Fermi GBM. *Astrophys. J.* **2020**, *891*, 70. [CrossRef]
6. Awaki, H.; Baring, M.G.; Bose, R.; Braun, D.; Casey, J.; Chun, S.; Galchenko, P.; Gau, E.; Goya, K.; Hakamata, T.; et al. XL-Calibur measurements of polarized hard X-ray emission from the Crab. *Mon. Not. R. Astron. Soc.* **2025**, *540*, L34–L40. [CrossRef]
7. Kole, M.; De Angelis, N.; Berlato, F.; Burgess, J.M.; Gauvin, N.; Greiner, J.; Hajdas, W.; Li, H.C.; Li, Z.H.; Pollo, A.; et al. The POLAR gamma-ray burst polarization catalog. *Astron. Astrophys.* **2020**, *644*, A124. [CrossRef]
8. Jelinek, J.; Bergmann, B.; Smolyanskiy, P. Evaluation of Timepix3 with a 1 mm thick silicon sensor as a Compton imaging polarimeter in the hard X-ray band. *J. Instrum.* **2025**, *20*, C02006. [CrossRef]
9. Poikela, T.; Plosila, J.; Westerlund, T.; Campbell, M.; Gaspari, M.D.; Llopart, X.; Gromov, V.; Kluit, R.; van Beuzekom, M.; Zappon, F.; et al. Timepix3: A 65K channel hybrid pixel readout chip with simultaneous ToA/ToT and sparse readout. *J. Instrum.* **2014**, *9*, C05013. [CrossRef]
10. Agostinelli, S.; Allison, J.; Amako, K.; Apostolakis, J.; Araujo, H.; Arce, P.; Asai, M.; Axen, D.; Banerjee, S.; Barrand, G.; et al. Geant4—A simulation toolkit. *Nucl. Instrum. Methods Phys. Res. Sect. A Accel. Spectrometers Detect. Assoc. Equip.* **2003**, *506*, 250–303. [CrossRef]
11. Spannagel, S.; Wolters, K.; Hynds, D.; Alipour Tehrani, N.; Benoit, M.; Dannheim, D.; Gauvin, N.; Nürnberg, A.; Schütze, P.; Vicente, M. Allpix2: A modular simulation framework for silicon detectors. *Nucl. Instrum. Methods Phys. Res. Sect. A Accel. Spectrometers Detect. Assoc. Equip.* **2018**, *901*, 164–172. [CrossRef]
12. Chauvin, M.; Friis, M.; Jackson, M.; Kawano, T.; Kiss, M.; Mikhalev, V.; Ohashi, N.; Stana, T.; Takahashi, H.; Pearce, M. Calibration and performance studies of the balloon-borne hard X-ray polarimeter PoGO+. *Nucl. Instrum. Methods Phys. Res. Sect. A Accel. Spectrometers Detect. Assoc. Equip.* **2017**, *859*, 125–133. [CrossRef]
13. Bergmann, B.; Gohl, S.; Garvey, D.; Jelínek, J.; Smolyanskiy, P. Results and Perspectives of Timepix Detectors in Space—From Radiation Monitoring in Low Earth Orbit to Astroparticle Physics. *Instruments* **2024**, *8*, 17. [CrossRef]
14. Granja, C.; Polansky, S.; Vykydal, Z.; Pospisil, S.; Owens, A.; Kozacek, Z.; Mellab, K.; Simcak, M. The SATRAM Timepix spacecraft payload in open space on board the Proba-V satellite for wide range radiation monitoring in LEO orbit. *Planet. Space Sci.* **2016**, *125*, 114–129. [CrossRef]
15. Stefan, G. Timepix Detector in Space Applications and Radiation Belt Dynamics Observed at Low Altitudes. Ph.D. Thesis, Charles University, Prague, Czech Republic, 2024.

16. Urban, M.; Doubravová, D. Timepix3: Temperature influence on X-ray measurements in counting mode with Si sensor. *Radiat. Meas.* **2021**, *141*, 106535. [CrossRef]
17. Urban, M.; Nentvich, O.; Marek, L.; Hudec, R.; Sieger, L. Timepix3: Temperature Influence on Radiation Energy Measurement with Si Sensor. *Sensors* **2023**, *23*, 2201. [CrossRef] [PubMed]
18. Farkas, M.; Bergmann, B.; Broulim, P.; Burian, P.; Ambrosi, G.; Azzarello, P.; Pušman, L.; Sitarz, M.; Smolyanskiy, P.; Sukhonos, D.; et al. Characterization of a Large Area Hybrid Pixel Detector of Timepix3 Technology for Space Applications. *Instruments* **2024**, *8*, 11. [CrossRef]
19. Sykorova, K.; Buk, Z.; Cepek, M.; Granja, C.; Oancea, C.; Marek, L. Machine learning models for single-particle classification with Timepix 3 detector. *J. Instrum.* **2025**, *20*, C01028. [CrossRef]
20. Harrison, F.A.; Craig, W.W.; Christensen, F.E.; Hailey, C.J.; Zhang, W.W.; Boggs, S.E.; Stern, D.; Cook, W.R.; Forster, K.; Giommi, P.; et al. The Nuclear Spectroscopic Telescope Array (NuSTAR) High-Energy X-Ray Mission. *Astrophys. J.* **2013**, *770*, 103. [CrossRef]
21. Aleksić, J.; Ansoldi, S.; Antonelli, L.; Antoranz, P.; Babic, A.; Bangale, P.; Barrio, J.; Becerra González, J.; Bednarek, W.; Bernardini, E.; et al. Measurement of the Crab Nebula spectrum over three decades in energy with the MAGIC telescopes. *J. High Energy Astrophys.* **2015**, *5–6*, 30–38. [CrossRef]
22. Abarr, Q.; Beheshtipour, B.; Beilicke, M.; Bose, R.; Braun, D.; de Geronimo, G.; Dowkontt, P.; Errando, M.; Gadson, T.; Guarino, V.; et al. Performance of the X-Calibur hard X-ray polarimetry mission during its 2018/19 long-duration balloon flight. *Astropart. Phys.* **2022**, *143*, 102749. [CrossRef]
23. Turecek, D.; Jakubek, J.; Trojanova, E.; Sefc, L. Compton camera based on Timepix3 technology. *J. Instrum.* **2018**, *13*, C11022. [CrossRef]
24. Turecek, D.; Jakubek, J.; Trojanova, E.; Sefc, L. Single layer Compton camera based on Timepix3 technology. *J. Instrum.* **2020**, *15*, C01014. [CrossRef]
25. Amoyal, G.; Schoepff, V.; Carrel, F.; Michel, M.; Blanc de Lanaute, N.; Angélique, J. Development of a hybrid gamma camera based on Timepix3 for nuclear industry applications. *Nucl. Instrum. Methods Phys. Res. Sect. A Accel. Spectrometers Detect. Assoc. Equip.* **2021**, *987*, 164838. [CrossRef]
26. Wen, J.; Zheng, X.; Gao, H.; Zeng, M.; Zhang, Y.; Yu, M.; Wu, Y.; Cang, J.; Ma, G.; Zhao, Z. Optimization of Timepix3-based conventional Compton camera using electron track algorithm. *Nucl. Instrum. Methods Phys. Res. Sect. A Accel. Spectrometers Detect. Assoc. Equip.* **2022**, *1021*, 165954. [CrossRef]
27. Smolyanskiy, P.; Bergmann, B.; Burian, P.; Cherlin, A.; Jelínek, J.; Maneuski, D.; Pospíšil, S.; O'Shea, V. Characterization of a 5 mm thick CZT-Timepix3 pixel detector for energy-dispersive γ-ray and particle tracking. *Phys. Scr.* **2024**, *99*, 015301. [CrossRef]
28. Kamtchou, B.; León Vintró, L.; Cournane, S. An experimental and computational evaluation of a novel Timepix3 detector for Compton imaging in nuclear medicine. *J. Instrum.* **2024**, *19*, P12004. [CrossRef]

Disclaimer/Publisher's Note: The statements, opinions and data contained in all publications are solely those of the individual author(s) and contributor(s) and not of MDPI and/or the editor(s). MDPI and/or the editor(s) disclaim responsibility for any injury to people or property resulting from any ideas, methods, instructions or products referred to in the content.